Available online at www.sciencedirect.com
SCIENCE DIRECT®
Physica D 199 (2004) 82–90
PHYSICA D
www.elsevier.com/locate/physd

Patterns and localized structures in a hybrid non-equilibrium Ising model

L.M. Pismen*, M.I. Monine, G.V. Tchernikov[1]

Department of Chemical Engineering, Minerva Center for Nonlinear Physics of Complex Systems, Institute of Catalysis Science and Technology, Technion – Israel Institute of Technology, 32000 Haifa, Israel

Abstract

We study a hybrid non-equilibrium pattern formation model combining short-scale Ising model with a continuous slow or long scale inhibitor. The computation combines alternates Monte-Carlo algorithm with updating of the inhibitor field. It is very fast, and allows us to study the influence of various factors, such as scale ratios, coupling strength, bias, temperature (level of noise), anisotropy, etc., on the pattern formation and behavior of emerging non-equilibrium structures.

Keywords: Non-equilibrium patterns; Ising model; Monte-Carlo algorithm; Hybrid method

1. Introduction

Studies of symmetry breaking and pattern formation in non-equilibrium systems are commonly based on reaction–diffusion models [1,2]. A dazzling variety of patterns were obtained using either representative equations of Ginzburg–Landau type or ad hoc models, such as Brusselator or FitzHugh–Nagumo equations containing "activator" and "inhibitor" variables with widely separated spatial and temporal scales. Less common is a cellular automaton (CA) approach [3–6], where the activator is modeled by cell elements which can switch between a definite number of states (e.g. described by a binary variable $u = \{0, 1\}$) in such a way that the state of any element at a given time step is determined by the states of this element and its neighbors at the previous step. Recent interest to pattern formation on microscopic and nanoscopic scales, especially in surface restructuring and catalysis [7], brought about more intricate models explicitly including intermolecular interactions: nonlocal "mesoscopic" models and various applications of Monte-Carlo (MC) techniques. Both reaction–diffusion modeling and MC computations become technically difficult and lose computational efficiency under conditions (rather typical for surface reactions and transport), when characteristic times and diffusional ranges of different species are widely separated. In reaction–diffusion computations this necessitates introducing fine grid fitting the short-

* Corresponding author. Tel.: +972 4 829 3086; fax: +972 4 823 0476.
E-mail address: pismen@tx.technion.ac.il (L.M. Pismen).
[1] Present address: Division of Computational Mathematics, Moscow State University of Communications (MIIT), Obraztsova Street 15, Moscow, 127994, Russia.

0167-2780/$ – see front matter © 2004 Elsevier B.V. All rights reserved.
doi:10.1016/j.physd.2004.08.006

est relevant scale. Practical considerations dictate using modest scale ratios in numerical studies of model equations of FitzHugh–Nagumo (FN) type [8], which makes it difficult to compare numerical results with analytical results obtained in the "sharp interface" limit when the scale ratio tends to infinity [9–13]. MC computations are short-scale by their nature and cannot be extended to a macroscopically large region at reasonable cost. Moreover, they are very sensitive to disparity of characteristic times of alternative transitions that causes waste of computing time in simulations based on a common importance-sampling algorithm . CA computations are more flexible in this respect, as they allow for different averaging kernels and distinct dynamic algorithms for "activator" and "inhibitor" particles [5,6].

Our choice is a *hybrid* model that combines MC computations for a fast short-scale component of the model with a continuous description of a long-scale or slow component. Hybrid computations of this kind have been recently applied in modeling of CO oxidation on Pt(1 1 0) , where the main emphasis was on realistic description of surface reconstruction and roughening coupled to kinetic oscillations. The aim of the present communication is different: setting up a simple and versatile model enabling us to study qualitative features of non-equilibrium patterns. The model described below can be viewed as a hybrid version of the FN model. The latter exists in two versions: the original version with a fast activator and slow non-diffusing inhibitor that generates propagating waves, and the version with a long-scale inhibitor that generates Turing patterns and solitary spots. The behavior of hybrid counterparts of both models is discussed in Sections 4 and 5.

Our model is very much different from the cellular automaton version of the FN model in Ref. [14] where MC dynamics imitated fictitious reactions formally generating respective reaction–diffusion equations according to the mass action law. It differs as well from CA models [4–6] where cells were modeled as excitable elements "firing" with a probability depending on their neighborhood and, in later models, modified by mobile inhibitor particles. [5,6]. Aiming at the simplest possible scheme, we use the classical two-state Ising model as a symbolic analog of an activator species in a bistable reaction–diffusion equation. The connection between these two models is discussed in Section 2. The non-equilibrium model is set up (Section 3) by coupling with either slow diffusionless or long-scale diffusive inhibitor equation, and the results of computations are discussed in Sections 4 and 5.

2. Continuous and discrete equilibrium models

The Ising model can be viewed as a discrete analog of the nonlinear reaction–diffusion equation (called also real Ginzburg–Landau or Allen–Cahn model)

$$u_t = \nabla^2 u + u - u^3, \tag{1}$$

where all coefficients have been rescaled to unity. A generalized asymmetric dimensional form of this equation can be derived from the energy functional

$$F = \int L \,\mathrm{d}\boldsymbol{x}, \qquad L = \tfrac{1}{2}K|\nabla u|^2 + V(u) + \epsilon W(u), \tag{2}$$

where K is rigidity coefficient, V is a symmetric double-well potential, and W is an antisymmetric correction, which is scaled by $\epsilon \ll 1$ to make its action comparable to that of surface tension for structures of a characteristic size large compared to the effective interface thickness. The evolution equation

$$\chi^{-1} u_t = K\nabla^2 u - V'(u) - \epsilon W'(u) \tag{3}$$

is derived from (2) by applying the dissipative dynamics principle $u_t = -\chi\delta F/\delta u$, where χ is mobility coefficient. Eq. (1) with time scaled by $(\chi T_0)^{-1}$ and length by $\sqrt{K/T_0}$ corresponds to the particular case $V(u) = 1/4T_0(1-u^2)^2$, $W(u) = 0$, where T_0 is an appropriate energy scale. The bias potential can be chosen in such a way that it does not affect the position of equilibria, e.g. $W(u) = T_0 u(1 - 1/3u^2)$.

The simplest discrete analog of Eq. (1) is MC computation of transitions between two alternative states $u = \pm 1$ on a square lattice with transition probabilities

$$p = \min\{\tfrac{1}{2}\mathrm{e}^{-[E]/T},\ 1\}, \tag{4}$$

where $[E]$ is the change of energy resulting from a flip of u. In the symmetric case E is proportional to the number n ($0 \le n \le 4$) of nearest neighbors with a different value of u; the proportionality constant is the interaction coefficient $J > 0$. If the energies of the alternative states are biased by some value $2\epsilon E_0$, the energy of a single cell is computed as

$$E = \epsilon u E_0 + Jn. \tag{5}$$

A comparison between the continuous and discrete equilibrium models can be found in a recent publication [15]. The correspondence between the two is established by comparing the characteristic length and time scales, which are all of $O(1)$ when the continuous model is scaled as in Eq. (1) and the length and time units coincide, respectively, with the cell size and Monte-Carlo cycle (MCC), i.e. the time interval wherein one transition attempt occurs, on the average, in each cell. More precisely, MCC can be identified with the characteristic time $\tau = (\chi|V''(u_0)|/u_0)^{-1}$ computed for some representative value of u_0, say that corresponding to one of the stationary states, e.g. $\tau^{-1} = 2\chi T_0$ for the symmetric quatric potential, or $\tau = 1/2$ for the dimensionless model (1).

The rigidity coefficient in the dimensional continuous model (3) equivalent to the MC algorithm is computed by comparing the the surface energy of a planar interface separating "up" and "down" domains

$$\sigma_0 = K\int_{-\infty}^{\infty} u'(x)^2\,\mathrm{d}x = \sqrt{\frac{KT_0}{2}}\int_{-1}^{1}(1-u^2)\,\mathrm{d}u = \tfrac{2}{3}\sqrt{2KT_0}. \tag{6}$$

with the Onsager surface tension [16]

$$\sigma_1 = J\left(2 - \frac{T}{J}\ln\coth\frac{J}{T}\right). \tag{7}$$

This gives the correspondence $\sqrt{2KT_0} = 3J$ at zero temperature. The decrease of surface tension at higher temperatures leading to an effective interface widening and increased fluctuations does not have a counterpart in a continuous deterministic model. The latter defines only the intrinsic interface width, while MC computation based on the Ising model gives also interface widening due to capillary waves. With growing fluctuations, the surface tension vanishes at $T/J > 2.269$, and the "up" and "down" phases cease to be separated beyond this point.

3. Hybrid non-equilibrium models

A non-equilibrium hybrid model imitating the FN system is constructed by making the bias energy E_0 dependent on the "inhibitor" field v described by a reaction–diffusion equation. In the simplest version, $E_0 = v$ and the equation of v is linear. We shall consider two hybrid models. In the first model (Section 4), the inhibitor is slow and non-diffusing and obeys locally the dynamic equation

$$\gamma^{-1}v_t = -v - \nu + \mu u, \tag{8}$$

where ν, μ are, respectively, bias and coupling parameters and γ^{-1} is the characteristic time. Since v can be rescaled, the relevant parameters are the products $\epsilon\nu$, $\epsilon\mu$. Computations using Eqs. (4), (5) and (8) are carried out by alternately updating the values of the binary variable $u = \pm 1$ during one MCC and updating the values of the continuous variable v in each cell by itegrating Eq. (8) using the fourth-order Runge-Kutta method during the time interval Δt, which is identified with the duration of MCC. In the second model (Section 5), the inhibitor is rapidly diffusing and obeys the linear reaction–diffusion equation with a diffusivity $\epsilon^{-2}D$ large compared to the $O(1)$ effective diffusivity of the binary variable.

$$\gamma^{-1}v_t = \epsilon^{-2}D\nabla^2 v - v - \nu + \mu\langle u\rangle, \tag{9}$$

where $\langle\cdots\rangle$ denotes averaging over an area large compared to the Ising cell size. This equation is solved on a "macrogrid" with the units of ϵ^{-1} size; the inhibitor values on the macrogrid nodes are updated alternately with MCC updates of u, using the alternating-direction implicit scheme [17]. The values of u are averaged over each macrogrid unit. The boundary conditions are periodic in all computations.

4. Diffusionless model

The diffusionless model based on Eq. (8) simulates excitable behavior at moderate values of the coupling parameter μ and oscillatory behavior when coupling is very strong. A simulation run for a symmetric case ($\nu = 0$) starting from uniform $v = 0$ and random initial values of u shows, after a short coarsening stage, a dynamic fluctuating pattern seen in Fig. 1. The snapshots in Fig. 1 are taken from computations at different temperatures. One can observe significant nucleation noise (seen as flickering of single cells in "hostile" surroundings) at high temperatures, while at low temperatures grid-induced anisotropy causes predominant alignment of domain boundaries along the coordinate axes. Mid-

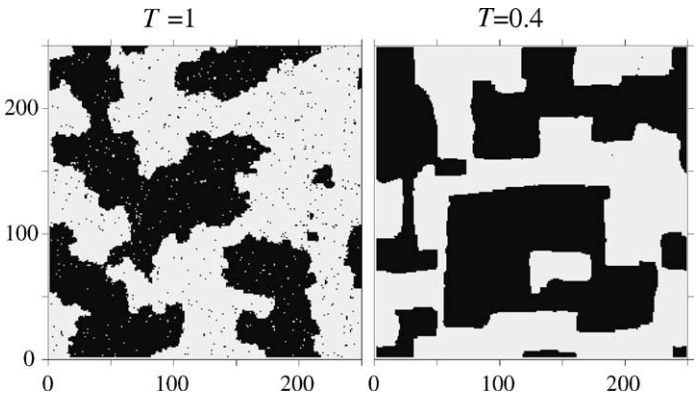

Fig. 1. Snapshots of patterns of the binary variable u obtained at high and low temperatures. Black areas correspond to $u = -1$, and white, to $u = 1$. Initial conditions: $v(x, y) = 0$ and $u(x, y)$ distributed randomly between -1 and 1. Parameters: $\gamma\,\Delta t = 0.006$, $\epsilon\mu = 0.14$, $\nu = 0$, $J = 1$. Grids for u and v: 250×250 nodes.

temperature runs are most representative as analogs of a continuous system with added noise. The average domain size increases with decreasing $\gamma\,\Delta t$, as seen by comparing Fig. 2(a) and (b). The patterns of the binary variable u in these figures have been obtained in long simulation runs at different values of $\gamma\,\Delta t$. The change of a typical domain size is expressed quantitatively by the energy plots in Fig. 2(c).

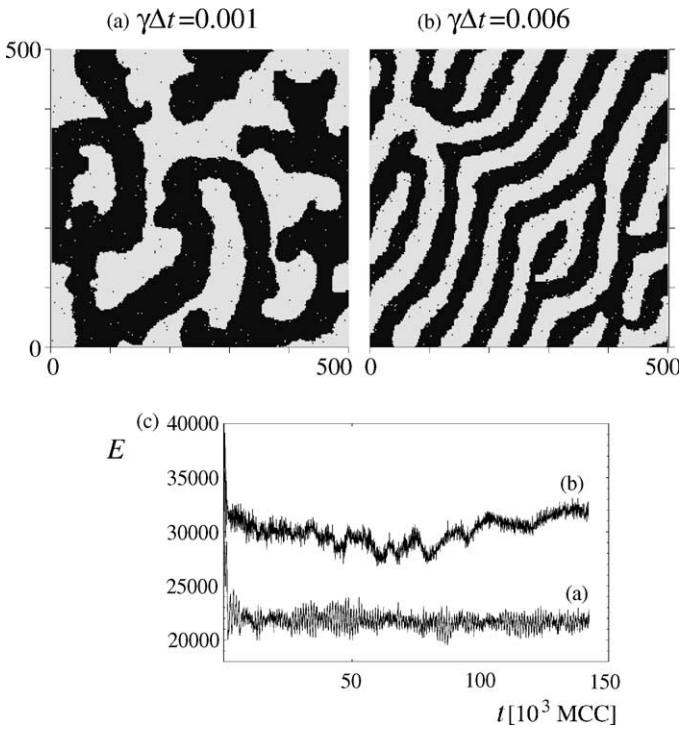

Fig. 2. Snapshots of patterns of the binary variable u obtained at high and low temperatures. Black areas correspond to $u = -1$, and white, to $u = 1$. Initial conditions: $v(x, y) = 0$ and $u(x, y)$ distributed randomly between -1 and 1. Parameters: $T = 0.8$, $\epsilon\mu = 0.14$, $\nu = 0$, $J = 1$. Grids for u and v: 500×500 nodes.

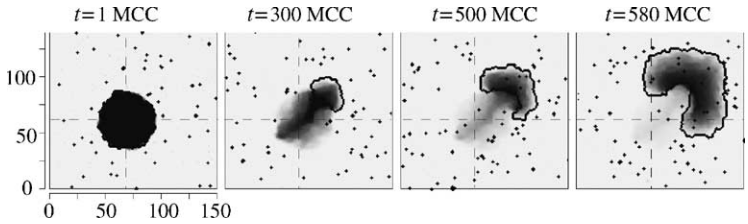

Fig. 3. Snapshots of a moving spot at a moderate temperature. The levels of the inhibitor field v are shown in gray scale (dark area, low v; light area, high v). The interphase boundary for the binary variable is shown by black contour ($u = -1$ inside the spot, $u = 1$ outside; crosses mark "defects", single cells with $u = -1$ in the $u = 1$ area). Initial conditions: $v(x, y) = 0$, $u = -1$ inside and $u = 1$ outside a circular spot. Parameters: $\gamma\,\Delta t = 0.006$, $\epsilon\mu = 0.14$ $\nu = 0$, $J = 1$, $T = 0.8$. Grids for u and v: 250×250 nodes.

While the number of cells in the "up" and "down" state remains approximately equal, the domains shift perpetually due to a slow drift of the level of the inhibitor v in each cell in the direction unfavorable to its current state. The direction of shift of domain boundaries is history-dependent at each location. This is seen by comparing the consecutive snapshots in Fig. 3. The boundary of the "down" state, shown by the solid line, advances where it passes through the region $v > 0$ (shown in lighter gray level) and recedes where it passes through the region $v < 0$ (shown in darker gray level). This, in turn, depends on the history of the respective locations, which, in the former case, had long been in the "up" and, in the latter case, in the "down" state.

The structures formed following a transition between alternative states of the binary variable localized in a compact region are typical for excitable systems. The snapshots in Fig. 3 show evolution starting from a spot of the "down" state. The spot is set into motion in a direction randomly selected under the influence of fluctuations, and keeps moving into the region of large v widening into a boomerang shape and leaving behind a relaxation trail of large v.

More distinct spiral waves are obtained in an asymmetric system with $\nu > 0$, which introduces a bias in favor of negative values of v and, hence, the "up" state of u. This causes the regions of "down" state to be relatively narrow. Patterns of broken and distorted spiral waves typical for these conditions are shown in Fig. 4; take note that the excited domains become thicker when the inhibitor slows down, i.e. at smaller values of $\gamma\,\Delta t$.

5. Coupling to long-scale inhibitor

The Ising model coupled to long-scale inhibitor generates Turing patterns and solitary objects similar to the

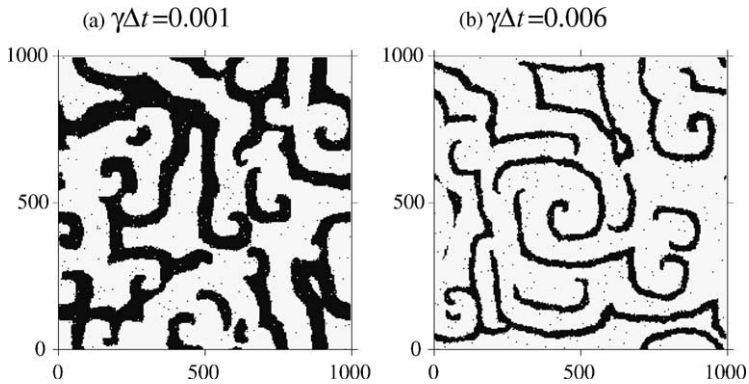

Fig. 4. A distorted spiral wave pattern of the binary variable u obtained at moderate temperatures with a non-zero bias parameter ν and different values of $\gamma\,\Delta t$. Black areas correspond to $u = -1$, white $u = 1$. Initial conditions: $v(x, y) = 0$ and $u(x, y)$ is distributed randomly between -1 and 1. Parameters: $\epsilon\mu = 0.14$, $\epsilon\nu = 0.03$, $J = 1$, $T = 0.8$. Grids for u and v: 1000×1000.

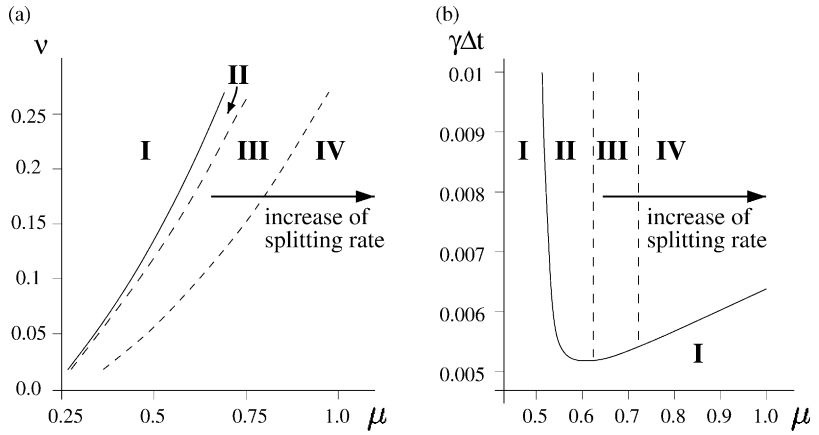

Fig. 5. Diagrams in the (μ, ν) and $(\mu, \gamma\,\Delta t)$ planes showing different dynamical behaviour in a system with a long-scale inhibitor. Initial conditions: $v(x, y) = -1$, $u = -1$ inside and $u = 1$ outside a circular spot. Fixed parameters: $\epsilon = 0.2$, $J = 1$, $T = 1$, $D = 1$; $\gamma\,\Delta t = 0.1$ (a), $\nu = 0.15$ (b).

reaction–diffusion model (1), (9), but shows a larger variety of behavior due to the impact of intrinsic noise. Fig. 5(a) summarizes the results of a number of simulation runs at different values of μ and ν and fixed values of other parameters and with identical initial conditions, with the "down" state inside a circle of a fixed radius and the "up" state elsewhere. Four parametric domains with distinct dynamic behavior are distinguished here:

I The spot disappears—no non-uniform asymptotic states.
II A wandering and breathing spot persists.
III "Wormlike" moving segments persist.
IV "Worms" grow, branch out, and split, leading to a distorted striped or labyrinthine pattern.

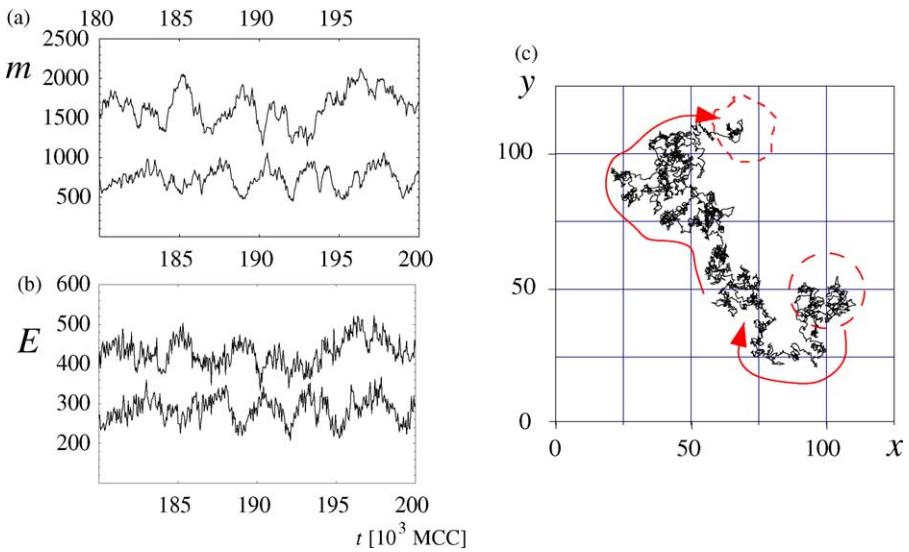

Fig. 6. Fluctuations of the area m (a) and interfacial energy E (b) of a wandering spot (Region II) at different inhibitor diffusivities: $D = 12.5$ (upper curves) and $D = 6.25$ (lower curves). (c) Trajectory of the center of mass of the spot at $D = 6.25$. Parameters: $\epsilon = 0.2$, $J = 1$, $T = 1$, $\mu = 0.55$ $\nu = 0.15$; u-grid: 250×250 nodes; v-grid: 50×50 nodes.

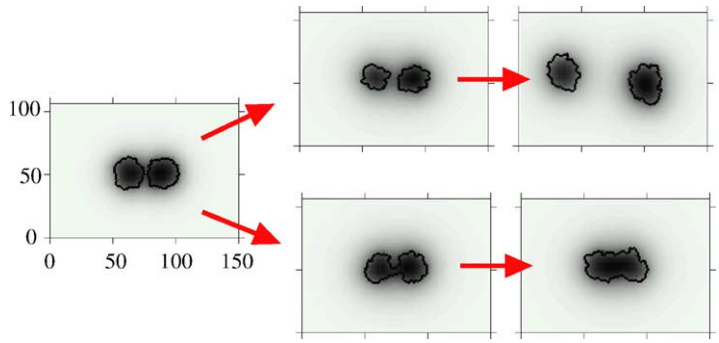

Fig. 7. Two scenarios for interacting spots under conditions corresponding to Region II. The levels of the inhibitor field v are shown in gray scale (dark area, low v; light area, high v). The interphase boundary for the binary variable is shown by black contour ($u = -1$ inside the spots, $u = 1$ outside). Parameters: $\epsilon = 0.2$, $J = 1$, $T = 14$,D=6.254, $\mu = 0.55$, $\nu = 0.15$; u-grid: 250 × 250 nodes; v-grid: 50 × 50 nodes.

A similar diagram in the plane (μ, $\gamma\,\Delta t$) is shown in Fig. 5(b). As in the reaction–diffusion model, coupling to the inhibitor acts, generally, in the way opposite to the action of surface tension. As a result, formation of stretched structures and splitting are favored at larger μ. Patterned states disappear when the response of the inhibitor becomes too slow.

It should be noted that the diagrams in Fig. 5 do not exhaust the variety of behavior of the hybrid model, which may be additionally modified by changing temperature and the scale ratio ϵ. The boundaries between the Regions I–IV are approximate, as, due to the intrinsic noise, transitions between different types of behavior are smooth and there are no sharp bifurcation lines. In all computations described in this Section, nucleation of single cells with a state differing from all four neighbors is suppressed. This does not significantly influence the dynamic behavior, except elimi-

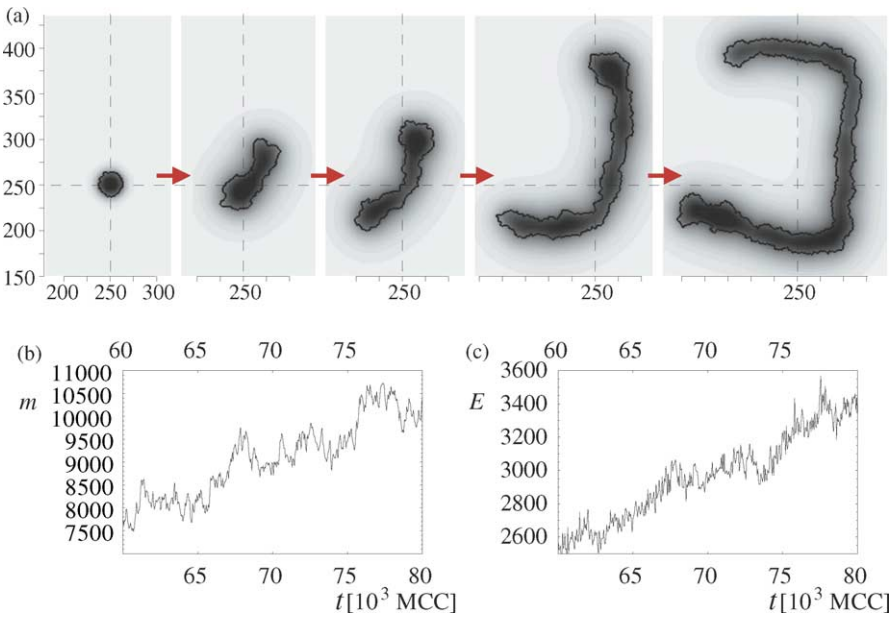

Fig. 8. (a) Snapshots showing evolution of a “worm" under conditions corresponding to Region III. The levels of the inhibitor field v are shown in gray scale (dark area, low v; light area, high v). The interphase boundary is shown by black contour ($u = -1$ inside the worm, $u = 1$ outside). (b,c) Fluctuations of the area m and interfacial energy E of the worm. Parameters: $\epsilon = 0.2$, $J = 1$, $T = 1$, $D = 6.25$, $\mu = 0.65$, $\nu = 0.15$; u-grid: 500 × 500 nodes; v-grid: 100 × 100 nodes.

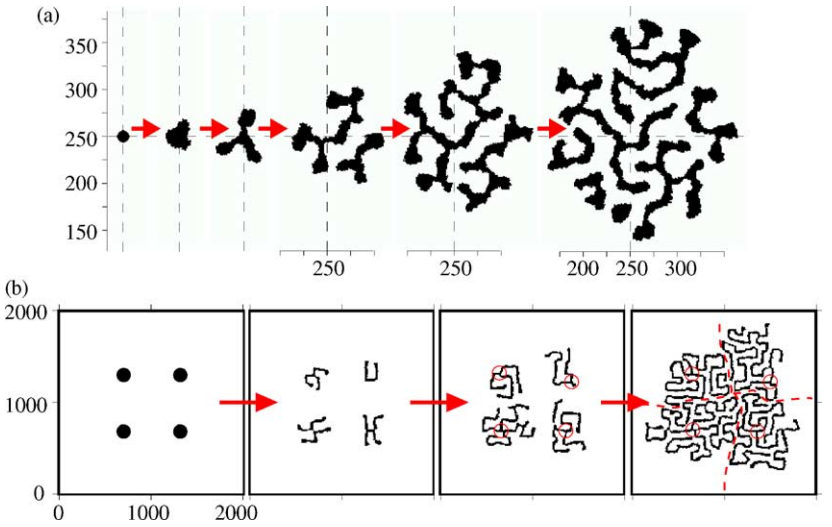

Fig. 9. Snapshots of patterns of the binary variable u obtained under conditions corresponding to Region IV. Black areas correspond to $u = -1$, and white, to $u = 1$. Parameters: $\epsilon = 0.2$, $J = 1$, $D = 6.25$, $\mu = 0.9$, $\nu = 0.15$. (a) A segmented pattern obtained through repeated splitting of a large spot at a high temperature ($T = 1$); u-grid: 500×500 nodes; v-grid: 100×100 nodes. (b) A labyrinthine pattern obtained starting from four large spots at a low temperature ($T = 0.7$); u-grid: 2000×2000 nodes; v-grid: 400×400 nodes.

nating "flickering" far from interphase boundaries, but considerably speeds up the computation.

One can see in Fig. 6 that the size and interfacial energy of a wandering spot in Region II remain, on the average, constant, while the spot undergoes Brownian motion in the plane. This solitary structure is an analog of a stationary, rather than a moving spot in the FN system; there is no persistent direction of motion, and no apparent asymmetry in the shape of the spot and distribution of the inhibitor in its surroundings. The position, as well as size fluctuations are caused by the intrinsic noise and decrease with growing spot size at larger values of the inhibitor diffusivity. This is not obvious in plots of absolute values of the area and interfacial energy in Fig. 6(a) and (b), but is revealed by comparing the standard deviations $(\langle m^2\rangle - \langle m\rangle^2)/\langle m\rangle^2 = 0.0302$ for $D = 6.25$ and 0.0172 for $D = 12.5$.

Fig. 7 illustrates interaction of two spots, which may, under identical conditions, either attract and merge or repel, dependent on the random factors.

The dynamics of a typical "worm" in Region III is illustrated by Fig. 8 showing evolution starting from a circular spot and growing gradually into a wandering and bending stripe. In Region IV "worms" branch out and divide, spreading gradually into a pattern covering the entire plane. The same pattern can be formed

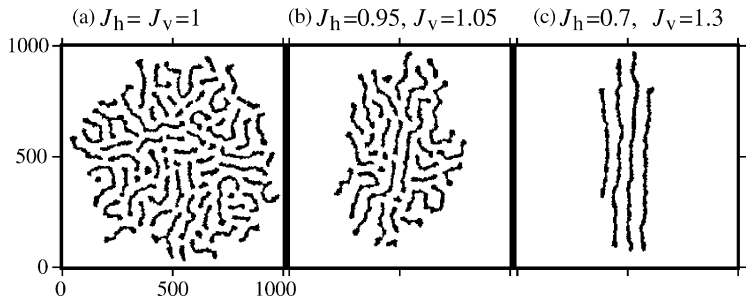

Fig. 10. Effect of anisotropic interactions. Black areas correspond to $u = -1$, and white, to $u = 1$. (a) Isotropic structure; (b) weak anisotropy; (c) strong anisotropy. Parameters: $\epsilon = 0.2$, $T = 1$, $D = 6.25$, $\mu = 0.65$, $\nu = 0.15$; u-grid: 1000×1000 nodes; v-grid: 200×200 nodes.

as a result of repeated splitting of a large spot, followed by spreading and multiplication of "worms". At higher temperatures, repeated splitting, leads to a segmented pattern, as in Fig. 9(a). At lower temperatures, splitting is suppressed, and persistent growth and branching leads to a labyrinthine pattern, as in Fig. 9(b). Take note that the patches grown out of four spots in this computation remained separated, since splitting of domains occupied by the background "up" state, requiring activation, is also suppressed at low temperatures.

Fig. 10 illustrates the effect of anisotropic interactions with J different for nearest neighbor cells in the "vertical" and "horizontal" directions. The computations were carried out under splitting conditions (Region IV). As anisotropy grows, splitting is suppressed, and the stripes stretch along the direction with a higher interaction strength in a way similar to that observed in reaction–diffusion computations [18].

6. Conclusions

The models described above reproduce principal features of the non-equilibrium reaction–diffusion models of FN type, but show a wider variety of behavior due to the influence of intrinsic noise. The hybrid algorithm is very fast, and allows us to study the influence of various factors, such as scale ratios, coupling strength, bias, temperature (level of noise), anisotropy, etc., on the pattern formation and behavior of emerging non-equilibrium structures.

Acknowledgment

This work has been supported by the German–Israeli Science Foundation. LMP acknowledges the support of Israel National Science Foundation and the EU and NATO ASI (PHYSBIO program) during the preparation stage of this manuscript.

References

[1] M.C. Cross, P.C. Hohenberg, Rev. Mod. Phys. 65 (1993) 851.
[2] E. Meron, Phys. Rep. 218 (1992) 1.
[3] A.S. Mikhailov, Foundations of Synergetics I, second ed., Springer, Berlin, 1994.
[4] P. Jung, G. Mayer-Kress, Phys. Rev. Lett. 74 (1995) 2130.
[5] H. Hempel, T. Fricke, L. Schimansky-Geier, in: J. Parisi, S.C. Mueller, W. Zimmermann (Eds.), Nonlinear Physics of Complex Systems, Springer, Berlin, 1996.
[6] H. Hempel, L. Schimansky-Geier, J. Garcia-Ojalvo, Phys. Rev. Lett. 82 (1999) 3713.
[7] R. Imbihl, G. Ertl, Chrm. Rev. 95 (1995) 679;
M. Hildebrand, A.S. Mikhailov, J. Phys. Chem. 100 (1996) 19089;
D.G. Vlachos, M.A. Katsoulakis, Phys. Rev. Lett. 85 (2000) 3898;
R. Imbihl, A.E. Reynolds, D. Kaletta, Phys. Rev. Lett. 67 (1991) 275;
R.J. Gelten, A.P.J. Jansen, R.A. van Santen, J.J. Lukkien, J.P.L. Segers, P.A.J. Hilbers, J. Chem. Phys. 108 (1998) 5921;
V.P. Zhdanov, B. Kasemo, J. Chem. Phys. 114 (2001) 5351;
V.P. Zhdanov, Surf. Sci. Rep. 287 (2002) 1;
E. Christoffersen, P. Stoltze, J.K. Nørskov, Surf. Sci. 505 (2002) 200;
M.I. Monine, L.M. Pismen, Cat. Today 70 (2001) (2001);
M.I. Monine, L.M. Pismen, Phys. Rev. E 66 (2002) 051601;
D.P. Landau, K. Binder, A Guide to Monte-Carlo Simulation in Statistical Physics, Cambridge University Press, Cambridge, 2000.
K. Krischer, A. Mikhailov, Phys. Rev. Lett. 73 (1994) 3165.
[8] C.P. Schenk, M. Or-Guil, M. Bode, H.-G. Purwins, Phys. Rev. Lett. 78 (1997) 3781.
[9] T. Ohta, M. Mimura, R. Kobayashi, Physica (Amsterdam) D 34 (1989) 115.
[10] L.M. Pismen, J. Chem. Phys. 101 (1994) 3135.
[11] C.B. Muratov, V.V. Osipov, Phys. Rev. E 53 (1996) 3101.
[12] R.E. Goldstein, D.J. Muraki, D.M. Petrich, Phys. Rev. E 53 (1996) 3933.
[13] L.M. Pismen, Phys. Rev. Lett. 86 (2001) 548.
[14] A. Malevanets, R. Kapral, Phys. Rev. E 55 (1997) 5657.
[15] P. Liu, M.T. Lusk, Phys. Rev. E 66 (2002) 061603.
[16] L. Onsager, Phys. Rev. 65 (1944) 117.
[17] W.H. Press, S.A. Teukolsky, W.T. Vetterling, B.P. Flannery, Numerical Recipes in C, second ed., Cambridge University Press, 1992.
[18] M. Bär, A. Hagberg, E. Meron, U. Thiele, Phys. Rev. E 62 (2000) 366.